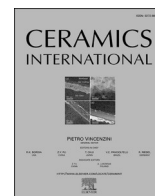




Contents lists available at ScienceDirect

Ceramics International

journal homepage: [www.elsevier.com/locate/ceramint](http://www.elsevier.com/locate/ceramint)

# pH dependent morphology and texture evolution of ZnO nanoparticles fabricated by microwave-assisted chemical synthesis and their photocatalytic dye degradation activities

M. Arellano-Cortaza<sup>a</sup>, E. Ramírez-Morales<sup>a</sup>, U. Pal<sup>b</sup>, G. Pérez-Hernández<sup>a</sup>, L. Rojas-Blanco<sup>a,\*</sup><sup>a</sup> Universidad Juárez Autónoma de Tabasco, Avenida Universidad S/n Zona de La Cultura, Colonia Magisterial, CP 86690, Villahermosa Centro, Tabasco, Mexico<sup>b</sup> Instituto de Física, Benemérita Universidad Autónoma de Puebla, Apartado Postal J-48, CP 72570, Puebla, Pue, Mexico

## ARTICLE INFO

## Keywords:

Microwave assisted synthesis  
pH control  
ZnO nanoparticles  
Photocatalysis

## ABSTRACT

ZnO nanostructures are well-known photocatalysts for the degradation of toxic organic dyes and their morphology, size, and other physicochemical properties play important roles in their photocatalytic performance. To study the effect of size, morphology, and synthesis conditions in photocatalytic performance, we synthesized ZnO nanoparticles of different morphologies through a simple microwave-assisted chemical process at different pH values of the reaction mixture. Different pH values of the reaction mixture produced ZnO nanoparticles of different morphologies and sizes. The nature of the pH controlling agent and final pH of the reaction mixture were seen to have considerable effects on the lattice parameters and microstrain of the ZnO nanocrystals, along with their photocatalytic performance. We observed that while the ZnO nanostructures synthesized at very high pH values of the reaction mixture have a high specific surface area, their photocatalytic activity is higher when they are synthesized at acidic pH or pH near the isoelectric point of ZnO. The results demonstrate that the photocatalytic activity of ZnO nanostructures not only depends on their size or specific surface area but also strongly depends on the concentration of catalytic sites at their surface.

## 1. Introduction

Population growth and subsequent increased energy demand of the present world along with insufficient environmental awareness of the people have increased water pollution to a level of considerable concern [1–3].

The release in effluents of unutilized chemical and biological agents from textile, wood, chemical, and pharmaceutical industries containing organic dyes, unutilized chemical and biological agents are the principal causes of present water pollution. All these compounds and biological agents are hazardous not only to marine or aquatic lives but also for surrounding wildlife and public health [4–6]. Among the above-mentioned contaminants released through industrial effluents, organic dyes of ionic or neutral nature such as Methylene Blue (MB), Rhodamine B (RhB), and Auramine O are the main components of textile and wool industry effluents, which, dissolved in water, reduce its oxygen content, causing the death of aquatic animals such as fishes and various microorganism. The presence of dyes in water bodies can also have various human effects depending on the degree of exposure since some

compounds are highly toxic and carcinogenic [7].

Several strategies have been adopted for eliminating organic dyes from wastewater, which include physical, biological, and chemical methods. Membrane-filtration processes, aerobic microbial degradation and chemical oxidation using Fenton's reagents are some of the popular methods. While these strategies cannot remove the contaminants completely, they generate equally toxic sub-products. Advanced oxidation processes (AOP) are a promising technology for dye degradation because they can generate highly reactive hydroxyl radicals (OH·) in large numbers and thus complete the oxidation of many pollutants, generating carbon dioxide, water, acid, or mineral salts as by-products [8]. Photo-active semiconductors, especially metal oxides have been utilized as catalysts in AOP processes. The use of metal oxides as photocatalysts in AOP has become relevant due to their high activity and stability, as well as low cost, and non-toxicity [9]. In AOP, the semiconductor photocatalyst is illuminated with visible or UV radiation of energy equal to or greater than its bandgap energy to produce electrons and holes. The photo-generated electron-hole pairs reach the surface of the semiconductor catalyst and are responsible for the redox reactions

\* Corresponding author.

E-mail addresses: [lizethrb@gmail.com](mailto:lizethrb@gmail.com), [lizeth.rojas@ujat.mx](mailto:lizeth.rojas@ujat.mx) (L. Rojas-Blanco).<https://doi.org/10.1016/j.ceramint.2021.06.170>

Received 6 November 2020; Received in revised form 25 May 2021; Accepted 21 June 2021

Available online 24 June 2021

0272-8842/© 2021 Elsevier Ltd and Techna Group S.r.l. All rights reserved.

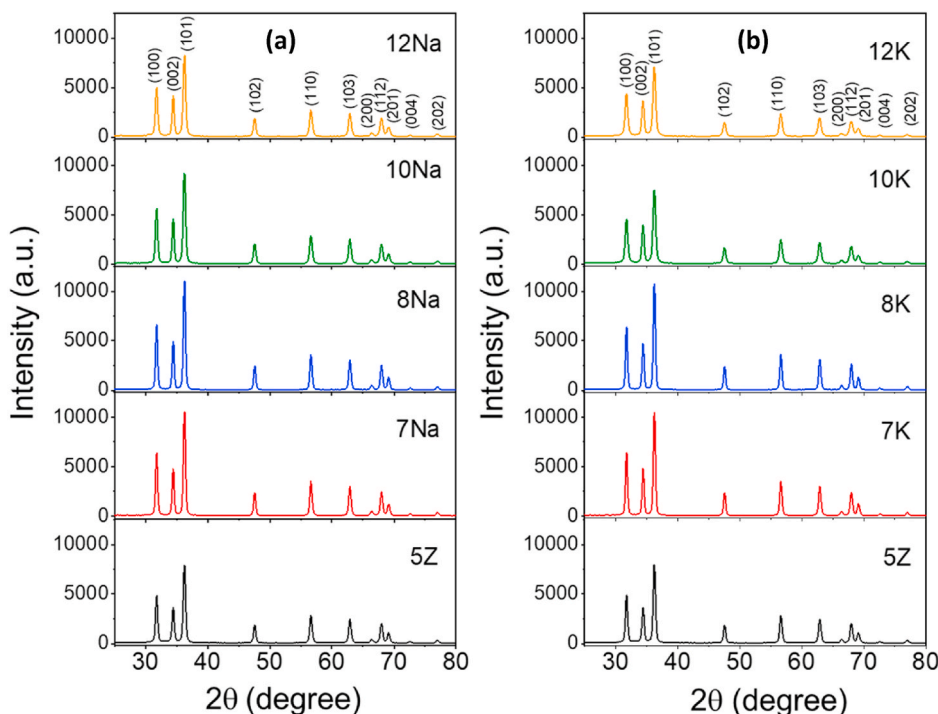


Fig. 1. XRD patterns of the ZnO nanostructures synthesized using a) NaOH and b) KOH as pH controlling agent in the reaction mixture.

that degrade contaminants [10]. During the process, the holes oxidize the water molecules and hydroxyl ions present on the surface, generating hydroxyl radicals and superoxide oxygen radical anions, while electrons and oxygen react to produce superoxide radical anions. These highly reactive species produced through redox reactions are responsible for degrading pollutants [11].

One of the most used metal oxide semiconductors in photocatalytic processes is  $\text{TiO}_2$ . However, ZnO is another metal oxide semiconductor that has higher photosensitivity and hence a greater capacity to generate hydroxyl radicals along with higher electron mobility than  $\text{TiO}_2$ . Recently nanostructured ZnO has become a widely used material in optoelectronic and environmental applications. The factors that play important roles in the photocatalytic performance of ZnO nanostructures are crystallite size, morphological, and textural properties of the particles, as well as Zn and O vacancy-related intrinsic defects. However, these properties can be controlled during the synthesis process by controlling the synthesis conditions such as reagents, solvents, precursor ratio, reaction time, and temperature [12]. Particularly, the number of structural defects in the ZnO particles can be increased through microwave-assisted synthesis due to the fast nucleation and growth involved in this process [13]. Also, microwave-assisted synthesis has a higher reaction efficiency and shorter synthesis time compared to synthesis by conventional heating [14].

ZnO nanostructures of different morphologies, crystallinity, and defect structures have been fabricated systematically utilizing different synthesis protocols. For example, Yu et al. [15] fabricated hierarchical 3D ZnO nanostructures using different surfactants (SDS, CTAB, PEG400, and PVP) in hydrothermal synthesis. Utilizing the hydrothermal process, Lin et al. [16] fabricated ZnO nanostructures of two different morphologies; one-dimensional scale-like ZnO (1D ZnO), and three-dimensional flower-like ZnO (3D ZnO), observing changes in photocatalytic performance when the nanostructures were annealed under hydrogen. Xu et al. [17] reported the fabrication of porous defective ZnO cellular hexagonal plates with high surface oxygen vacancies by hydrothermal and high-temperature  $\text{NaBH}_4$  reduction methods, which exhibited excellent solar-driven photocatalytic degradation performance. Mohammed and coworkers [18] synthesized

rods-like ZnO nanoparticles by MW-assisted reaction and utilized them for photocatalytic degradation of organic dyes. However, they did not consider the effects of the pH of the reaction-solution on the characteristics of ZnO particles. A few studies reported that modifying the pH in ZnO synthesis improves the photocatalytic activity without using a doping element [19,20]. Although ZnO nanostructures with different morphologies such as flowers, spheres, rods, leaves, prisms, hexagonal discs, etc. Have been reported in the literature, all of them have been synthesized in basic reaction media (pH 8–14) [21–23].

In the present work, ZnO nanostructures of different morphologies have been synthesized by microwave-assisted chemical technique at different pH values (acidic, basic, and neutral) of the reaction mixture. The nanostructures were prepared without adding any surfactant and without post-growth thermal treatment. Obtaining ZnO particles with oxygen vacancies and defects, due to the rapid reaction process and non-stoichiometric synthesis, is expected to improve their behavior in the degradation of pollutants. Morphology, structure, and optical properties of the nanostructures were evaluated using scanning electron microscopy (SEM), X-ray diffraction, micro-Raman, and UV-Vis spectroscopies. The Photocatalytic performance of the fabricated nanostructures was evaluated in the degradation of organic dyes under UV light.

## 2. Experimental

ZnO nanostructures were fabricated by microwave-assisted chemical synthesis. In a typical synthesis process, 0.4 mol of zinc acetate dihydrate ( $\text{Zn}(\text{CH}_3\text{COO})_2 \cdot 2\text{H}_2\text{O}$ , 99% Sigma Aldrich) was dissolved in 50 mL of ethanol ( $\text{C}_2\text{H}_5\text{OH}$ , 99.5%, Meyer) and 720  $\mu\text{L}$  of deionized water ( $\text{H}_2\text{O}$ ). The solution was kept under constant magnetic stirring for 10 min. The natural pH of the reaction mixture was 5.0. Then, the solution was placed inside an Anton Paar Multiwave PRO reactor and irradiated at 400 W for 10 min. The obtained product was washed with water and acetone several times and dried at 80 °C for 12 h. The sample obtained at this reaction pH (pH = 5) was denoted as 5Z. To study the effect of reaction pH, two more sets of samples were prepared at pH 7, 8, 10, and 12 of the reaction mixtures. The pH of the reaction mixture could be varied by the slow addition of either 4 M NaOH or 4 M KOH solutions (97%,

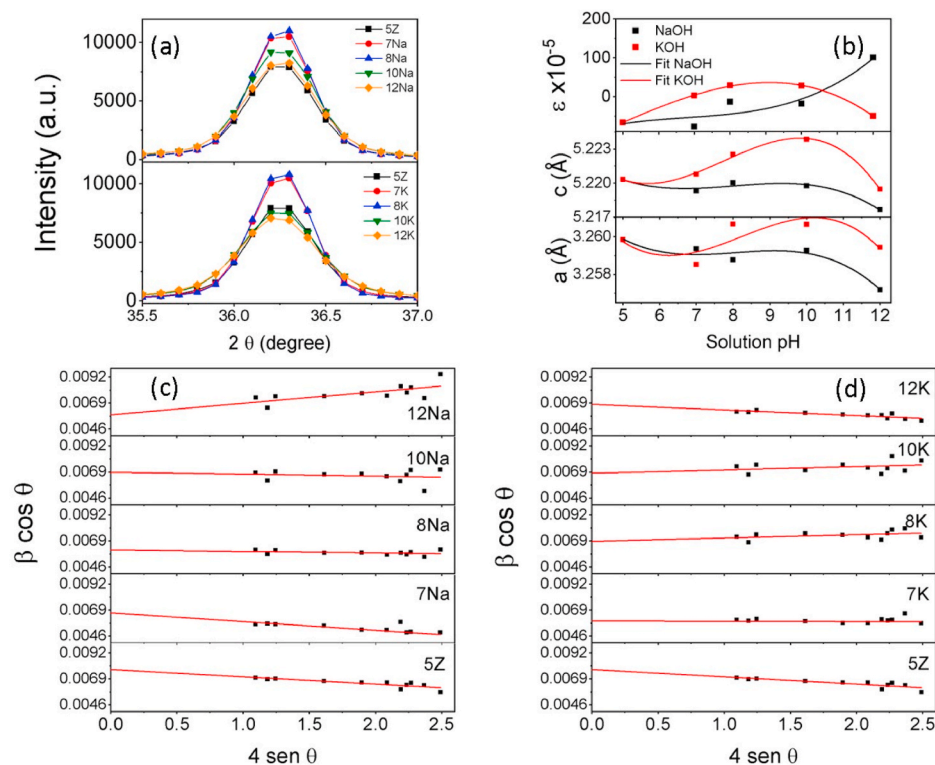


**Fig. 2.** (a) (101) diffraction peak of the ZnO nanostructures synthesized at different pH values utilizing NaOH and KOH as pH controlling agent, showing the variation of intensity and peak broadening; (b) variation of lattice parameters and micro-strain in the nanostructures with reaction pH prepared using NaOH and KOH; (c)  $4 \sin \theta$  vs.  $\beta \cos \theta$  plots using Williamson–Hall Uniform Deformation Model (UDM) analysis of the ZnO nanostructures prepared using NaOH, and (d)  $4 \sin \theta$  vs.  $\beta \cos \theta$  plots using Williamson–Hall Uniform Deformation Model (UDM) analysis of the ZnO nanostructures prepared using KOH as pH controlling agent.

CIVEQ) under magnetic stirring before their MW treatment. The samples prepared at pH 7, 8, 10, and 12 utilizing NaOH solution as pH adjusting agent were denoted as 7Na, 8Na, 10Na, and 12Na, respectively. Similarly, the samples prepared at pH 7, 8, 10, and 12 utilizing KOH solution as pH adjusting agent were denoted as 7K, 8K, 10K, and 12K, respectively. According to reports, both  $Zn^{2+}$  and  $OH^-$  sources have an important role in the final properties (optical, morphological, and structural) of photocatalysts, due to their nature and production processes, however, much remains to be clarified [24–27].

Obtained samples were structurally characterized by X-ray diffraction (XRD), using a Rigaku Smartlab diffractometer ( $\lambda_{CuK\alpha} = 1.544 \text{ \AA}$ ) The patterns were recorded with a scan rate of  $4.0^\circ/60.0 \text{ s}$ . Morphological analysis of the nanostructures was carried out in a field-emission scanning electron microscope (FESEM, JEOL InTouch Scope). Raman spectra of the samples were acquired at room temperature in a HORIBA Scientific (Xplora PLUS) micro-Raman spectrometer. A SHIMADZU Fourier spectrophotometer (FTIR IRAffinity-1S) was used to obtain the Fourier-transform infrared (FTIR) spectra of the samples in the  $4000\text{--}400 \text{ cm}^{-1}$  range. For FTIR measurements, the powder samples were pelletized with dry KBr (FT-IR grade, Sigma Aldrich). Surface area analysis of the samples was performed in a BELL Mini-II analyzer at

**Table 1**

XRD and BET estimated structural and texture parameters along with UV–Vis spectra analyzed band gap energy values of the ZnO nanostructures prepared at different reaction pH values utilizing NaOH and KOH as pH controlling agent.

Sample	Av. Crystallite size (nm)	$S_{BET}$ ( $\text{m}^2 \text{ g}^{-1}$ )	Av. pore size (nm)	$E_g$ (eV)
5Z	18	9.95	2.75	3.16
7Na	21	5.93	1.75	3.19
8Na	23	6.72	1.55	3.18
10Na	20	9.40	1.56	3.17
12Na	24	14.56	1.52	3.17
7K	23	5.94	1.57	3.19
8K	20	5.96	1.56	3.18
10K	20	6.44	1.56	3.15
12K	20	12.11	1.56	3.15

liquid nitrogen temperature. Before recording the adsorption-desorption isotherms, the samples were degassed at  $200^\circ \text{C}$  for 3 h under vacuum. The optical absorption spectra of the samples were obtained in a SHIMADZU UV-2600 spectrophotometer.

Methylene blue (MB,  $C_{16}H_{18}ClN_3S$ , 98.5%, CIVEQ) and rhodamine B (RhB,  $C_{28}H_{31}ClN_2O_3$ ) aqueous solutions (10 ppm) were used to evaluate the photocatalytic activity of the ZnO nanostructures. For photocatalytic evaluation, 24 mg of the catalyst was added into 80 mL of dye solution. Prior to irradiation, the solution was kept under ultrasonic stirring for 30 min to reach the adsorption-desorption equilibrium between the catalyst and the dye molecules. The lamp used in the experiments is a UVA light bulb, also known as black light, which emits a wavelength between 400 and 320 nm, with an approximate average of 365 nm. It should be noted that the lamp used is 30 W of power, which was fitted on the top of the glass reactor at 10 cm above the liquid level. The photocatalytic reaction was carried out for 240 min. To measure the changes in the concentration of the solution, aliquots ( $\sim 5 \text{ mL}$ ) were taken from the reaction mixture every 30 min and centrifuged (2500 rpm, 20 min) to separate the photocatalyst from the suspension. A SHIMADZU UV-2600 spectrophotometer was used to monitor the changes in absorbance in the main bands of MB and RhB, located at 664 and 554 nm, respectively.

### 3. Results and discussion

X-ray diffraction was used to investigate the crystal structure of the ZnO samples synthesized at different reaction pH, as shown in Fig. 1. All the samples revealed sharp and intense diffraction peaks correspond to the hexagonal wurtzite phase of ZnO (JCPDS Card # 36–1451). No additional peak corresponds to other phase or impurity in the diffraction patterns of the samples, indicating their high purity. However, with the variation of solution pH, changes in the intensity and peak broadness (Fig. 2a) could be observed for both the sample sets (prepared using NaOH and KOH as pH controlling agents).

Variations in the intensity and width of the diffraction peaks are associated with changes in the crystallite size and lattice strain of the

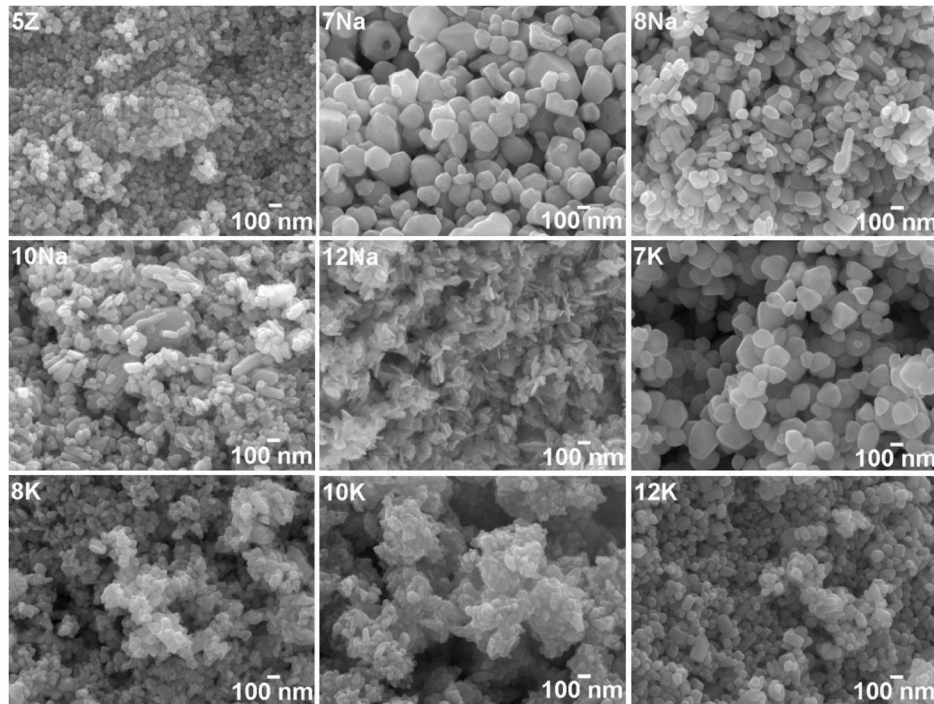


Fig. 3. Typical SEM images of the ZnO nanostructures synthesized at different reaction pH values using NaOH (series Na) and KOH (series K) as pH controlling agent.

structure [28,29]. Average crystallite size and lattice strain in the fabricated nanostructures were estimated utilizing the Uniform Deformation Model (UDM) of the Williamson-Hall, utilizing the relation [30]:

$$\beta \cos \theta = \frac{K\lambda}{D} + 4\epsilon \sin \theta \quad (1)$$

where  $K$  is a shape factor, which is  $\sim 0.9$  for spherical particles,  $\epsilon$  is the

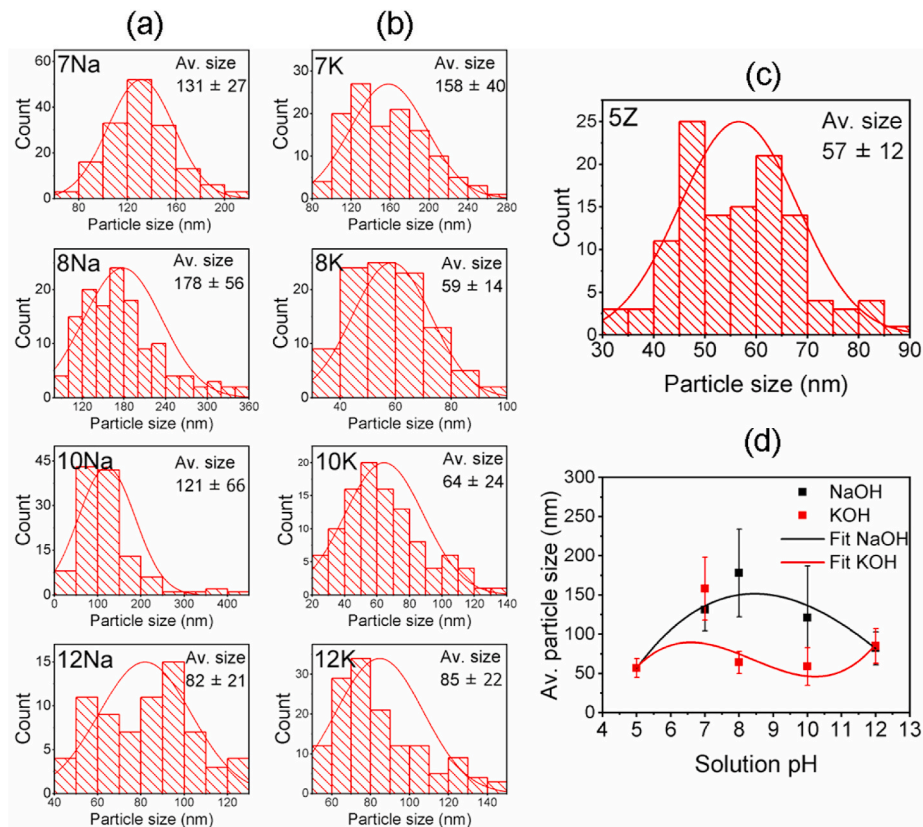


Fig. 4. Size distribution histograms and log-normal fittings of the particles in the samples prepared using (a) NaOH and (b) KOH as pH controlling agents; (c) size distribution histogram for the ZnO nanoparticles in sample 5Z; (d) variation of average particle size with solution pH for the two pH controlling agents.

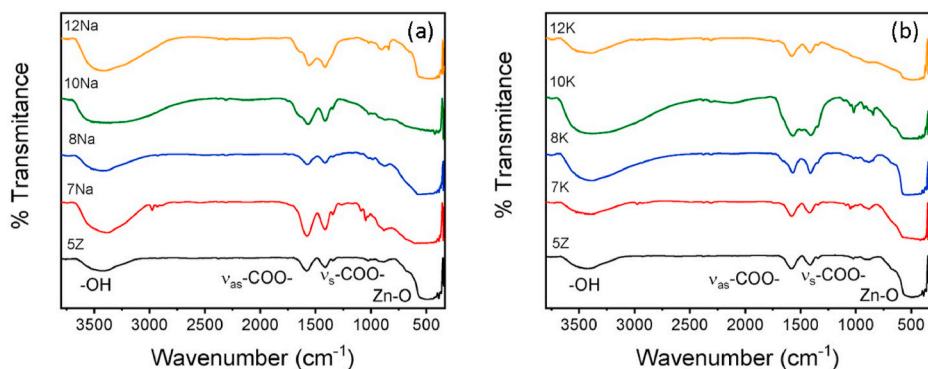


Fig. 5. Room temperature FTIR spectra of the ZnO nanostructures synthesized at different reaction pH values, using (a) NaOH and (b) KOH as pH controlling agent.

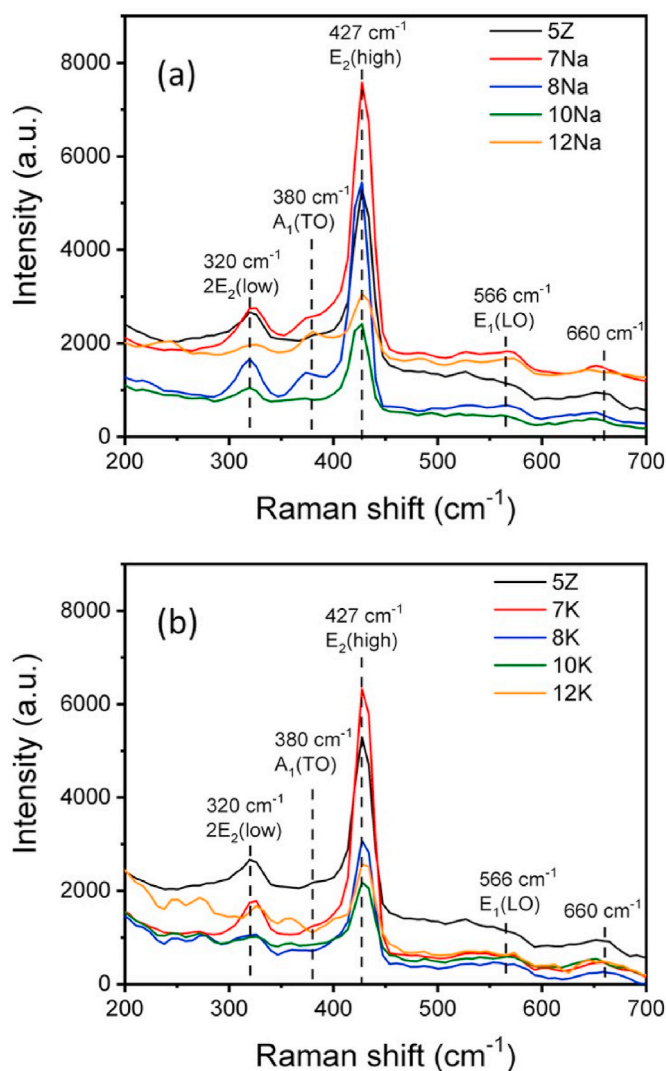


Fig. 6. Room temperature Raman spectra of the ZnO nanostructures synthesized using (a) NaOH and (b) KOH as pH controlling agent.

lattice strain,  $\beta$  is the full width at half maximum (FWHM) of the considered diffraction peak in radian,  $\theta$  is the Bragg's angle,  $\lambda$  is the X-ray wavelength, and  $D$  is the crystallite size. Using the slope and the intercept in the ordinate axis of the linear fits of the  $\beta \cos \theta$  vs  $4 \sin \theta$  plots, lattice strain and average crystallite sizes in the samples were estimated, respectively (Fig. 2c and d) [31]. Obtained results are summarized in Table 1.

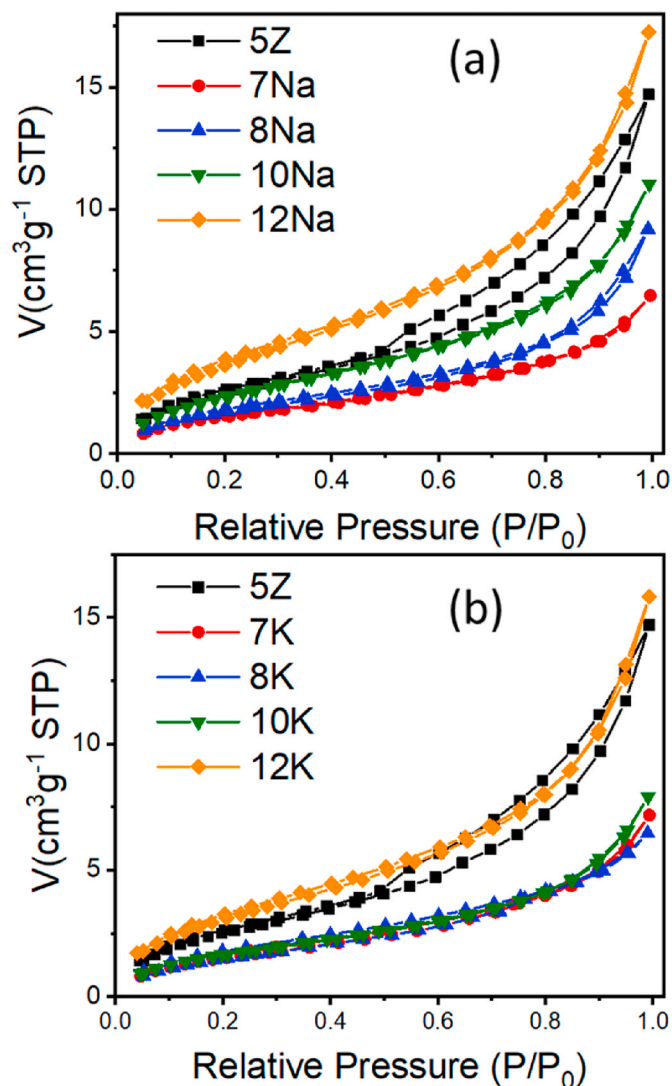


Fig. 7. N<sub>2</sub> adsorption-desorption isotherms of the ZnO nanostructures synthesized using (a) NaOH and (b) KOH as a pH controlling agent, recorded as 77 K.

Lattice parameters of the nanocrystals were calculated using the following equations [28]:

$$a = \frac{\lambda}{\sqrt{3} \sin \theta_{100}} \quad (2)$$

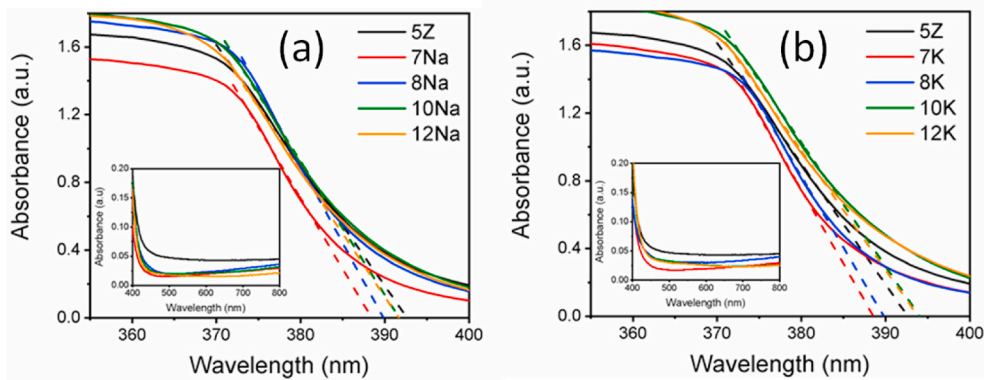


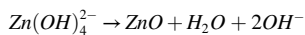
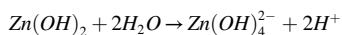
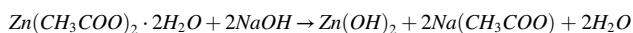
Fig. 8. UV-Vis optical absorption spectra of the ZnO nanostructures synthesized at different pH values using (a) NaOH and (b) KOH.

$$c = \frac{\lambda}{\sin \theta_{002}} \quad (3)$$

Fig. 2b shows the changes in lattice strain and lattice parameters of the ZnO particles with the variation of solution pH for both the cases (NaOH and KOH). As can be seen in Fig. 2b, for the case of NaOH as a pH controller, the lattice parameters  $a$  and  $c$  vary in a complex manner with clear  $a$ -axis lattice shrinkage and  $c$ -axis lattice expansion near a pH of 8.5, which is close to the isoelectric point of ZnO [32]. On the other hand, for KOH, after an initial shrinkage of the lattice both along  $a$  and  $c$ , the values of the lattice constants increased, reaching a maximum near pH = 9.5, indicating a lattice expansion along of both the  $a$  and  $c$ -axis. Observed changes in the lattice constants and lattice strain could be associated with the change in the reaction pH, as well as the source of hydroxyl ions used in the synthesis process since the type of base used has significant effects on the crystallinity and structural defects of the ZnO particles [25,26,33]. As can be seen, the lowest values of  $a$  and  $c$  were obtained using NaOH as a pH controlling agent, and the highest with KOH; these variations can be explained by Ralph Pearson's theory of hard acids and hard bases.  $\text{OH}^-$  is a hard base and prefers the union of a hard acid (the smaller the ions are the harder) and the hardness of the acid is reduced  $\text{Li} > \text{Na} > \text{K} > \text{Rb} > \text{Cs}$ . Therefore, the hydrolysis of Zn in KOH solution is faster than that of NaOH and its crystal growth rate is higher [34].

Similar results were reported by Abdelouhab et al. [35], where they indicate that the nature of zinc ions source precursor and the used alkaline hydroxide not only affect the crystallinity of the sample but also the morphology and size of particles. Uekawa et al. [36] reported that the interaction between cations in alkali metal hydroxide, water molecules, and  $\text{Zn}(\text{OH})_4^{2-}$  ions affect the growth process of zinc oxide crystals. With the increase of pH of the reaction medium, the average crystallite size of the ZnO particles changes (Table 1).

The possible growth of the ZnO particles is described by the following chemical reactions [37,38]:



In this work, KOH was also used as a source of hydroxyl ions so an above process similar would be carried out.

The morphology of the microwave synthesized ZnO nanostructures was investigated by scanning electron microscopy (SEM). Typical SEM images of the samples are shown in Fig. 3. As can be seen, the sample prepared without adjusting solution pH (i.e. without the addition of an alkaline agent, sample 5Z) consists of nanometric particles of semi-spherical shape. ZnO particles synthesized at reaction solution pH = 7 with NaOH addition (sample 7Na) contained a bit bigger particles of

semi-spherical shape, with prominent crystal facets. The shape of the particles changed from semi-spherical to rod-like for sample 8Na. For the reaction pH = 10 (i.e. sample 10Na), the particles become a bit smaller and non-uniform shapes. Finally, for reaction pH = 12, the shape of the obtained particles is disk-like.

On the other hand, for the samples synthesized using KOH as a pH controlling agent, for the sample prepared at pH = 7 (sample 7K) revealed similar morphology as that of the sample 7Na with a slightly bigger average size. However, for the samples prepared with higher solution pH, i.e., samples 8K, 10K, and 12K, the average size of the particles decreased gradually with shape becoming irregular (Fig. 4). Particle size distribution in the samples was analyzed by measuring the size of individual particles from the SEM micrograph of the respective sample, and the average particle size was estimated by the log-normal fitting of the size distribution histograms (Fig. 4). As can be seen in Fig. 4d, for both NaOH and KOH, with the increase of solution pH, average particle size increased up to a certain pH value and then decreased. While for NaOH, the maximum average particle size was for pH = 8, the maximum particle size for KOH was obtained at pH = 7.

Changes observed in crystallite size and morphology of the synthesized ZnO particles are related to the variations in the molar ratio  $\text{Zn}^{2+}$  and  $\text{OH}^-$  ions in the reaction solution [39], since the addition of NaOH and KOH have significant effects on the concentration of  $\text{Zn}(\text{OH})_2$  and  $[\text{ZnO}(\text{OH})_4]^{2-}$  present in the reaction medium, which controls the nucleation and growth rate of ZnO nanostructures [15]. The variation of  $\text{Zn}(\text{OH})_2$  and  $[\text{ZnO}(\text{OH})_4]^{2-}$  in the reaction mixture can also induce lattice strain, causing structural deformation. The results obtained in the present work indicate the role of reaction pH on the size and morphology of the ZnO nanostructures.

To confirm the existence of organic compounds and inorganic species in the ZnO nanostructures synthesized at different pH values, all the samples were characterized by FTIR spectroscopy in the range of 4000–400  $\text{cm}^{-1}$  (Fig. 5). The band that appeared at  $\sim 3400 \text{ cm}^{-1}$  is associated with the stretching vibration of  $-\text{OH}$ , which probably appeared due to the water adsorbed on the surface of the particles [40]. The sharp and well-defined absorption bands that appeared around 1580  $\text{cm}^{-1}$  and 1420  $\text{cm}^{-1}$  are the symmetric stretching ( $\nu_s\text{-COO}$ ) and asymmetric stretching ( $\nu_{as}\text{-COO}$ ) that are characteristic of the acetate groups [41]. Also, it is possible to observe signals around 900–1100  $\text{cm}^{-1}$  that are related to the acetate group [42], attributable to the precursors or the formation of by-products of the reaction, either as sodium acetate or potassium acetate [38]. The signals of these acetate groups were not eliminated because heat treatment was not performed on the samples obtained.

These species found on the surface of photocatalysts may affect the interaction with both dye and water molecules in the photocatalysis process. Finally, the characteristic vibrational modes of the Zn–O bond appeared in between 420 and 500  $\text{cm}^{-1}$ , confirming the formation of ZnO in the samples [43].

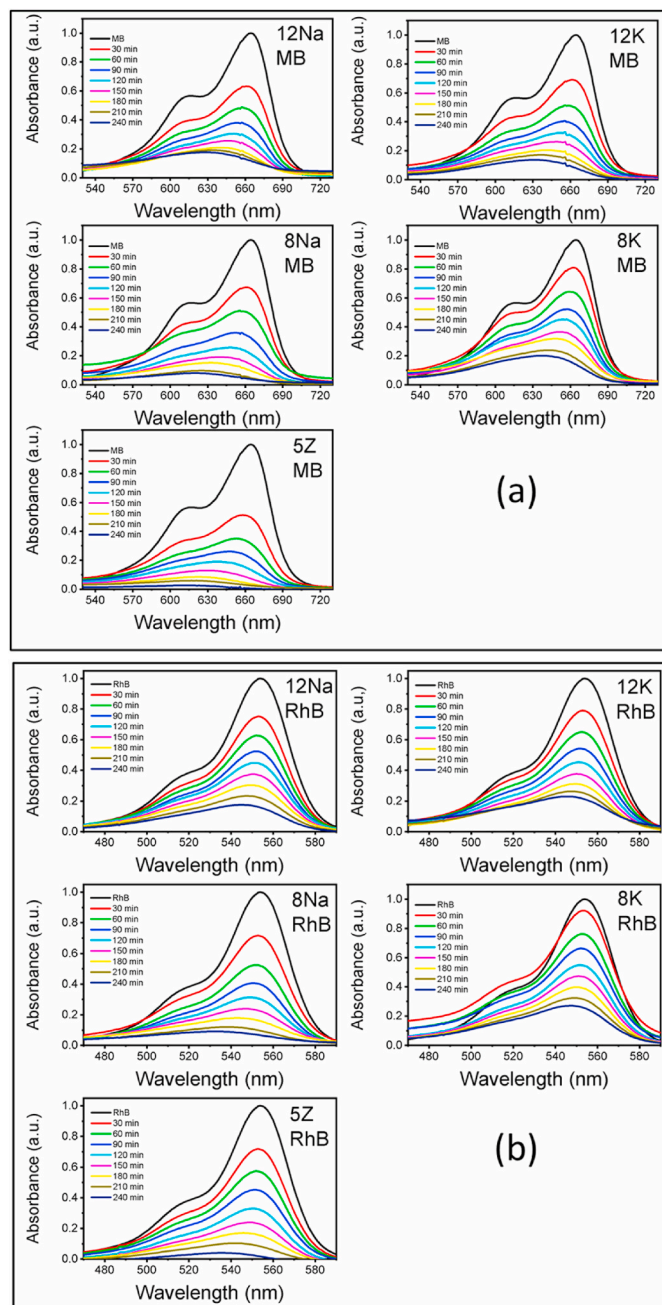


Fig. 9. Absorption spectra of the (a) MB and (b) RhB solution recorded at different intervals during photocatalytic degradation by ZnO nanostructures prepared using NaOH and KOH.

According to group theory, the wurtzite structure of ZnO (space group  $C_{6v}^4$ ) has 3 vibrational modes active in Raman;  $A_1$ ,  $E_1$ , and  $E_2$  [44]. Fig. 6 shows the Raman spectra of the samples synthesized with NaOH and KOH as a pH controlling agent. The strongest peak for all samples appeared around  $427\text{ cm}^{-1}$ , which is the  $2E_2$  (high) vibration mode of the nonpolar optical phonons of ZnO [45]. Two weak bands observed around  $313$  and  $380\text{ cm}^{-1}$  are the zero limit phonons  $2E_2$  (low) and the transverse optical mode  $A_1$  (TO), respectively [46]. The  $E_1$  (LO) mode appeared at  $566\text{ cm}^{-1}$  corresponds to the surface oxygen vacancies in ZnO [47]. Also, all samples present a signal  $\sim 660\text{ cm}^{-1}$  indicating the presence of the adsorbed acetate group [42], corroborating the observations in FTIR. The high intensity of the  $E_2$  mode together with the weak signal of  $E_1$  (LO) confirms that the synthesized ZnO nanostructures possess high crystallinity as indicated by the XRD results [44].

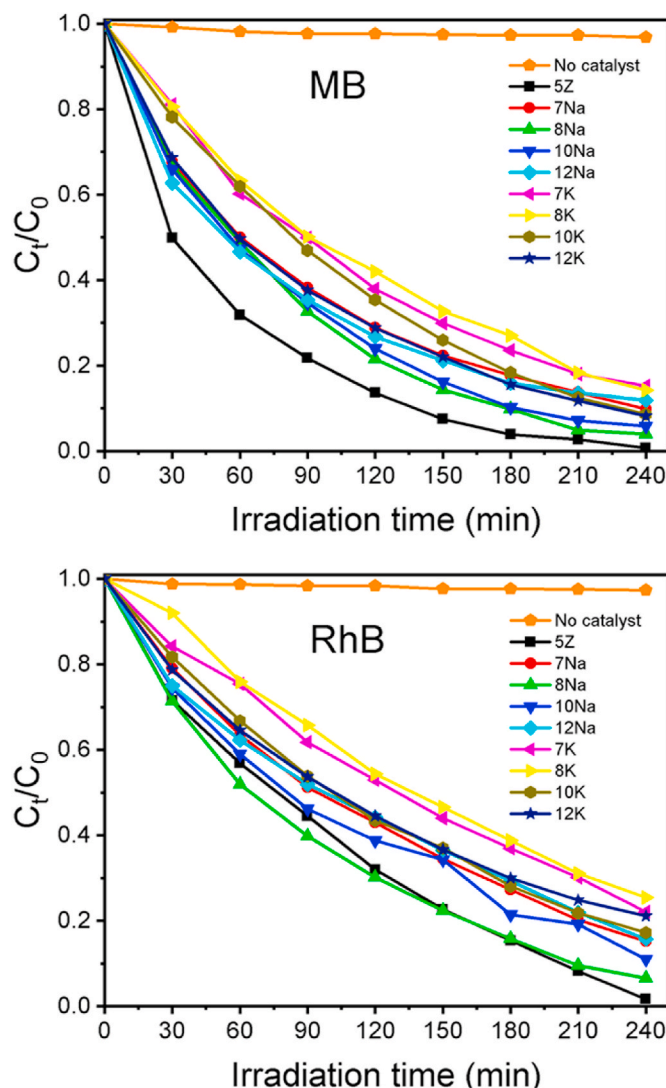


Fig. 10. Plot of  $(C_t/C_0)$  versus time for ZnO nanostructures synthesized at different pH values using NaOH and KOH, for the degradation of (a) MB and (b) RhB at different intervals of time.

To estimate the specific surface area of the ZnO samples synthesized at different reaction pH, their  $N_2$  adsorption-desorption isotherms were recorded at 77 K (Fig. 7). BET multipoint method was used on the lower relative pressure region of the adsorption isotherm to estimate the specific surface area. Pore size distribution in the samples was obtained using the BJH (Barret, Joyner, Halenda) method on the adsorption isotherm (Table 1). According to the IUPAC classification, all the samples show type IV adsorption isotherms with H3 hysteresis loops, characteristic of mesoporous materials [48,49]. Table 1 presents the specific surface area data calculated for all the samples. From Table 1, it can be seen that as the pH of the precursor solution increased, the specific surface area decreased (in general), which is in good agreement with the SEM observations, where the samples with the higher pH values revealed higher particle aggregation [50]. Also, the 5Z sample exhibited a larger pore size range compared to the other samples, allowing its greater specific surface area.

Fig. 8 shows the optical absorption spectra of ZnO particles synthesized at different pH values using NaOH and KOH as pH controlling agents. All the samples revealed a sharp absorption edge in the UV region (200–400 nm). However, the sample 5Z exhibited a slightly higher

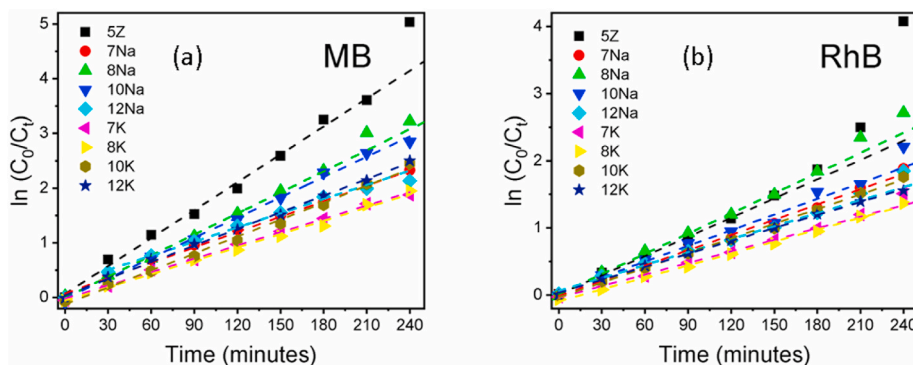


Fig. 11. Kinetics of (a) MB and (b) RhB degradation by the ZnO nanostructures prepared using NaOH and KOH as a pH controlling agent.

Table 2

Summary of photocatalytic performance of ZnO nanoparticles synthesized at different pH values of the reaction mixture. D corresponds to degradation % and k corresponds to kinetic constant.

Sample	MB		RhB	
	% D	$k$ ( $\text{min}^{-1}$ )	% D	$k$ ( $\text{min}^{-1}$ )
5Z	99	$17 \times 10^{-3}$	98	$9.5 \times 10^{-3}$
7Na	90	$9.4 \times 10^{-3}$	85	$7.6 \times 10^{-3}$
8Na	96	$12.8 \times 10^{-3}$	93	$11.1 \times 10^{-3}$
10Na	94	$12.3 \times 10^{-3}$	89	$7.8 \times 10^{-3}$
12Na	88	$8.6 \times 10^{-3}$	84	$6.7 \times 10^{-3}$
7K	85	$8.1 \times 10^{-3}$	78	$6.1 \times 10^{-3}$
8K	86	$8.1 \times 10^{-3}$	75	$5.9 \times 10^{-3}$
10K	91	$10.3 \times 10^{-3}$	83	$7.3 \times 10^{-3}$
12K	92	$10.1 \times 10^{-3}$	79	$6.4 \times 10^{-3}$

absorption in the visible region, unlike the other samples (inset). Bandgap energy values for the samples were estimated by extrapolating the linear portions of absorbance spectra ( $R \geq 0.998$ ), using the relation [51]:

$$E_g = \frac{1239.84 \times m}{-b} \quad (4)$$

where  $m$  and  $b$  correspond to the slope and intercept in the ordinate axis of the linear fits, respectively. The 5Z sample possesses a bandgap energy value of 3.16 eV, while 7Na, 8Na, 10Na, and 12 Na samples exhibited their bandgap energy as 3.19, 3.18, 3.17, and 3.17 eV, respectively. Samples prepared with KOH, i.e., 7 K, 8 K, 10 K, and 12 K revealed their bandgap energy values 3.19, 3.18, 3.15, and 3.15 eV, respectively.

Photocatalytic efficiencies of the ZnO nanoparticles were evaluated using methylene blue (MB) (10 ppm) and rhodamine B (RhB) (10 ppm) degradation as model reactions. For photocatalytic tests, 24 mg of catalyst was added to 80 mL of the dye solution. Before irradiation, the solution was placed in an ultrasonic bath under dark for 30 min, to obtain the adsorption-desorption equilibrium of the dye on the sample surface.

Photocatalytic degradation was carried out over 240 min using a UV lamp of 30 W power placed 10 cm above the reactor. After every 30 min of UV irradiation, an aliquot (approximately 5 mL) was withdrawn from the reaction solution and centrifuged to separate the particles. Change in absorbance of the catalyst-free aliquots was determined from their absorption spectra, monitoring the intensity of the principal absorption bands of MB and RhB located at 665 and 554 nm, respectively. The degradation efficiency (DE) was calculated using the relation:

$$DE(\%) = \frac{C_0 - C_t}{C_0} \times 100 = \frac{A_0 - A_t}{A_0} \times 100 \quad (5)$$

where  $C_0$ ,  $A_0$  correspond to the initial concentration and absorbance of

the dye, respectively.  $C_t$ ,  $A_t$  are the concentration and absorbance of the dye at time  $t$ , respectively [52,53].

Absorption spectra of the MB and RhB dye solutions at different times of UV exposure are shown in Fig. 9. It can be seen that the intensity of the main absorption bands of the dye molecules decreases gradually with irradiation time. However, the catalyst 5Z exhibits a higher degradation rate for both the dyes (Fig. 10). In the case of MB, the degradation efficiency after 240 min of irradiation was as follows: 5Z (99%) > 8Na (96%) > 10Na (94%) > 12K (92%) > 10K (91%) > 7Na (90%) > 12Na (88%) > 8K (86%) > 7K (85%). On the other hand, for RhB, the samples presented the following sequence of degradation: 5Z (98%) > 8Na (93%) > 10Na (89%) > 7Na (85%) > 12Na (84%) > 10K (83%) > 12K (79%) > 7K (78%) > 8K (75%).

For the tested dyes (MB & RhB), the 7 K and 8 K samples revealed the lowest percentage of degradation. We attribute this behavior to the fact that both the samples possess low specific surface area, in addition to their highest energy gap values among the samples.

$$\ln\left(\frac{C_0}{C_t}\right) = kt \quad (6)$$

Langmuir-Hinshelwood (L-H) kinetic model was used to calculate the kinetic constants of the samples for the photocatalytic degradation of MB and RhB. For that, we utilized the relation: Where  $C_0$  is the initial dye concentration,  $C_t$  is the dye concentration at time  $t$  and  $k$  is the pseudo-first-order rate constant. Fig. 11 shows  $\ln(C_0/C_t)$  versus time plots of the photocatalysts for MB and RhB degradation. The linear fits used for the determination of  $k$  values (rate constants) had a good fit to the data points ( $R^2 \geq 0.994$ ) and the rate constants values for the samples are listed in Table 2.

As can be seen in Table 2, samples 5Z and 8Na have the highest activities among the samples of corresponding groups for degrading MB and RhB, while samples 7K and 8K have the lowest activities. While the sample prepared with natural pH = 5.0 of the reaction mixture (i.e. the sample 5Z, prepared without adjusting pH) revealed the best photocatalytic activity for degrading MB and RhB, an increase of solution pH of the synthesis reaction mixture to 7.0 using either NaOH or KOH produced ZnO nanostructure of reduced photocatalytic activities. On increasing the pH of the reaction mixture further up to a certain level (i.e., up to pH = 8 for NaOH and pH = 10 for KOH), the photocatalytic activity of the synthesized ZnO nanostructures increased. The photocatalytic activity of the ZnO nanostructures prepared at reaction solution pH higher than optimum (pH = 8 for NaOH and pH = 10 for KOH) value reduced. The results obtained in our photocatalytic study of the ZnO nanostructures prepared at different reaction solution pH under microwave irradiation indicate the ZnO nanostructures prepared at acidic or near isoelectric point pH values are more suitable for photocatalytic degradation of organic dye molecules. As can be noticed from Table 1 and 2, although the samples 5Z, 8Na, and 10K revealed high photocatalytic activity, their specific surface areas are not the highest

among the samples of corresponding sets (prepared using NaOH or KOH). Rather, the nanostructures synthesized at the highest pH value (i. e. pH = 12.0) using either NaOH or KOH have the highest specific surface areas (Table 1). The results demonstrate that not only the specific surface area but the concentration of active catalytic sites at the surface plays an important role in the photocatalytic performance of the ZnO nanostructures.

That is, the active sites could be related to the oxygen vacancies of the 5Z sample, which are possible since the synthesis conditions are not stoichiometric [54], and due to the microwave irradiation the nucleation and growth of the crystals are done very quickly, promoting the increase of structural defects [18,55]. These defects cause the ZnO particles synthesized under acidic conditions to exhibit an increase in absorbance in the visible region [16,17,46], as shown in the inset in Fig. 8.

#### 4. Conclusion

In summary, we demonstrate the synthesis of ZnO nanoparticles of different morphologies through a fast, microwave-assisted chemical technique at different reaction pH values of the reaction mixture. While the nanoparticles of varied morphologies and sizes could be synthesized by the used technique, variation of reaction pH is seen to have a strong effect on the lattice parameters and lattice strain of ZnO nanocrystals. Depending on the nature of the pH controlling agent, lattice constants and microstrain of the ZnO nanocrystals lattice vary in complex manners. On utilizing NaOH as a pH controlling agent, both the lattice parameters *a* and *c* of the hexagonal ZnO lattice decrease with the increase of pH of the reaction mixture along with a gradual increase of microstrain; these changes in the values of *a* and *c* can be attributed to its basic dissociation constant, since being strong acids, it is possible that there is an excess of OH<sup>-</sup> ions, so there will be an accumulation of negative charges that generate a disaggregation.

However, on utilizing KOH as a pH controlling agent, both the lattice parameters increase with reaction pH along with the increase of lattice strain. While the ZnO nanostructures synthesized at the highest pH value (pH = 12) revealed the highest specific surface area, the nanostructures prepared at pH = 5 (natural pH value of the reaction solution) revealed the best photocatalytic performance of the degradation of organic dyes such as MB and RhB, clearly revealing the role of active catalytic sites at the nanostructure surface. We must consider that although the concentrations of Na<sup>+</sup> and K<sup>+</sup> on to the surface of ZnO particles could be low, the subproducts generated in the reaction (Na(CH<sub>3</sub>COO), K(CH<sub>3</sub>COO)) are possibly related to the discoloration percentages obtained in the tests [33], because the catalysts were not calcined.

So, these ions interact not only with the molecules of the organic dyes, but also with the water, and due to their properties, they affect the photocatalytic performance of the samples in which NaOH or KOH was used [32].

#### Declaration of competing interest

The authors declare that they have no known competing financial interests or personal relationships that could have appeared to influence the work reported in this paper.

#### Acknowledgements

UP acknowledges CONACyT, Mexico for the financial assistance through the project grant # A1-S-26720. Marcela Arellano Cortaza acknowledges CONACyT, Mexico, for financial support through the doctoral fellowship.

#### References

- [1] O.J. Guerra, G.V. Reklaitis, Advances and challenges in water management within energy systems, *Renew. Sustain. Energy Rev.* 82 (2018) 4009–4019, <https://doi.org/10.1016/j.rser.2017.10.071>.
- [2] P.J. Landrigan, R. Fuller, N.J.R. Acosta, O. Adeyi, R. Arnold, N.(Nil). Basu, A. B. Baldé, R. Bertollini, S. Bose-O'Reilly, J.I. Boufford, P.N. Breysse, T. Chiles, C. Mahidol, A.M. Coll-Seck, M.L. Cropper, J. Fobil, V. Fuster, M. Greenstone, A. Haines, D. Hanrahan, D. Hunter, M. Khare, A. Krupnick, B. Lanphear, B. Lohani, K. Martin, K. V Mathiasen, M.A. McTeer, C.J.L. Murray, J.D. Ndahimananjara, F. Perera, J. Potočnik, A.S. Preker, J. Ramesh, J. Rockström, C. Salinas, L. D. Samson, K. Sandilya, P.D. Sly, K.R. Smith, A. Steiner, R.B. Stewart, W.A. Suk, O. C.P. van Schayck, G.N. Yadama, K. Yumkella, M. Zhong, The Lancet Commission on pollution and health, *Lancet* 391 (2018) 462–512, [https://doi.org/10.1016/S0140-6736\(17\)32345-0](https://doi.org/10.1016/S0140-6736(17)32345-0).
- [3] H. Zhen, D.R. Ekman, T.W. Collette, S.T. Glassmeyer, M.A. Mills, E.T. Furlong, D. W. Kolpin, Q. Teng, Assessing the impact of wastewater treatment plant effluent on downstream drinking water-source quality using a zebrafish (*Danio Rerio*) liver cell-based metabolomics approach, *Water Res.* 145 (2018) 198–209, <https://doi.org/10.1016/j.watres.2018.08.028>.
- [4] Z. Vryzas, Pesticide fate in soil-sediment-water environment in relation to contamination preventing actions, *Curr. Opin. Environ. Sci. Heal.* 4 (2018) 5–9, <https://doi.org/10.1016/j.coesh.2018.03.001>.
- [5] W. Duan, F. Meng, H. Cui, Y. Lin, G. Wang, J. Wu, Ecotoxicity of phenol and cresols to aquatic organisms: a review, *Ecotoxicol. Environ. Saf.* 157 (2018) 441–456, <https://doi.org/10.1016/j.ecoenv.2018.03.089>.
- [6] S.T. Khan, A. Malik, Engineered nanomaterials for water decontamination and purification : from lab to products, *J. Hazard Mater.* 363 (2019) 295–308, <https://doi.org/10.1016/j.jhazmat.2018.09.091>.
- [7] S. Varjani, P. Rakholiya, H.Y. Ng, S. You, J.A. Teixeira, Microbial degradation of dyes: an overview, *Bioresour. Technol.* 314 (2020) 123728, <https://doi.org/10.1016/j.biortech.2020.123728>.
- [8] M. Sievers, Advanced oxidation processes, *Treatise Water Sci* 4 (2010) 377–408, <https://doi.org/10.1016/B978-0-444-53199-5.00093-2>.
- [9] A. Farroki, F. Feizpour, M. Asaadzadeh, Degradation of hazardous organic dyes with solar-driven advanced oxidation process catalyzed by the mixed metal-organic frameworks, *Appl. Organomet. Chem.* 33 (2019) 1–11, <https://doi.org/10.1002/aoc.4928>.
- [10] A. Fernandes, P. Makoš, Z. Wang, G. Boczkaj, Synergistic effect of TiO<sub>2</sub> photocatalytic advanced oxidation processes in the treatment of refinery effluents, *Chem. Eng. J.* 391 (2020) 123488, <https://doi.org/10.1016/j.cej.2019.123488>.
- [11] A. Mittal, B. Mari, S. Sharma, V. Kumari, S. Maken, K. Kumari, N. Kumar, Non-metal modified TiO<sub>2</sub> : a step towards visible light photocatalysis, *J. Mater. Sci. Mater. Electron.* 30 (2019) 3186–3207, <https://doi.org/10.1007/s10854-018-00651-9>.
- [12] N.M. Flores, U. Pal, R. Galeazzi, A. Sandoval, Effects of morphology, surface area, and defect content on the photocatalytic dye degradation performance of ZnO nanostructures, *RSC Adv.* 4 (2014) 41099–41110.
- [13] L.Y. Yang, S.Y. Dong, J.H. Sun, J.L. Feng, Q.H. Wu, S.P. Sun, Microwave-assisted preparation, characterization and photocatalytic properties of a dumbbell-shaped ZnO photocatalyst, *J. Hazard Mater.* 179 (2010) 438–443, <https://doi.org/10.1016/j.jhazmat.2010.03.023>.
- [14] D. Singh, C.S.A. Gopal, D. Kumar, N. Mahato, M.A. Quraishi, M.H. Cho, Microwave induced facile synthesis and characterization of ZnO nanoparticles as efficient antibacterial agents, *Mater. Discov.* 11 (2018) 19–25, <https://doi.org/10.1016/j.md.2018.05.001>.
- [15] H. wa Yu, J. Wang, X. an Yan, J. Wang, P. fei Cheng, C. juan Xia, Effect of surfactants on the morphology and photocatalytic properties of ZnO nanostructures, *Optik* 185 (2019) 990–996, <https://doi.org/10.1016/j.ijleo.2019.04.040>.
- [16] Y. Lin, H. Hu, Y.H. Hu, Role of ZnO morphology in its reduction and photocatalysis, *Appl. Surf. Sci.* 502 (2020) 144202, <https://doi.org/10.1016/j.apsusc.2019.144202>.
- [17] Y. Xu, H. Li, B. Sun, P. Qiao, L. Ren, G. Tian, B. Jiang, K. Pan, W. Zhou, Surface oxygen vacancy defect-promoted electron-hole separation for porous defective ZnO hexagonal plates and enhanced solar-driven photocatalytic performance, *Chem. Eng. J.* 379 (2020) 122295, <https://doi.org/10.1016/j.cej.2019.122295>.
- [18] R. Mohammed, M.E.M. Ali, E. Goma, M. Mohsen, Green ZnO nanorod material for dye degradation and detoxification of pharmaceutical wastes in water, *J. Environ. Chem. Eng.* 8 (2020) 104295, <https://doi.org/10.1016/j.jece.2020.104295>.
- [19] K. Rajar, A. Balouch, M.I. Bhangar, T.H. Sherazi, R. Kumar, Degradation of 4-Chlorophenol under sunlight using ZnO nanoparticles as catalysts, *J. Electron. Mater.* 47 (2018) 2177–2183.
- [20] G. Byzanski, A.P. Pereira, D.P. Volanti, C. Ribeiro, E. Longo, High-performance ultraviolet-visible driven ZnO morphologies photocatalyst obtained by microwave-assisted hydrothermal method, *J. Photochem. Photobiol. Chem.* 353 (2018) 358–367.
- [21] Y. Guan, H.Y. Yu, S.Y.H. Abdalkarim, C. Wang, F. Tang, J. Marek, W.L. Chen, J. Militky, J.M. Yao, Green one-step synthesis of ZnO/cellulose nanocrystalline hybrids with modulated morphologies and superfast absorption of cationic dyes, *Int. J.*

- Biol. Macromol. 132 (2019) 51–62, <https://doi.org/10.1016/j.jbiomac.2019.03.104>.
- [22] X. Zhao, M. Li, X. Lou, Sol-gel assisted hydrothermal synthesis of ZnO microstructures: morphology control and photocatalytic activity, *Adv. Powder Technol.* 25 (2014) 372–378, <https://doi.org/10.1016/j.apt.2013.06.004>.
- [23] B. Avci, Y. Caglar, M. Caglar, Controlling of surface morphology of ZnO nanopowders via precursor material and Al doping, *Mater. Sci. Semicond. Process.* 99 (2019) 149–158, <https://doi.org/10.1016/j.mssp.2019.04.028>.
- [24] O.O. Namal, E. Kalipci, Adsorption kinetics of methylene blue removal from aqueous solutions using potassium hydroxide (KOH) modified apricot kernel shells, *Int. J. Environ. Anal. Chem.* (2019) 1–17, <https://doi.org/10.1080/03067319.2019.1656721>.
- [25] E.K. Droepenu, B.S. Wee, S.F. Chin, K.Y. Kok, E.A. Asare, Synthesis and characterization of single phase ZnO nanostructures via solvothermal method: influence of alkaline source, *Biointerface Res. Appl. Chem.* 10 (2020) 5648–5655, <https://doi.org/10.33263/BRIAC103.648655>.
- [26] N. Preda, M. Enculescu, C. Florica, A. Costas, A. Evangelhidis, E. Matei, I. Enculescu, Morphology-controlled synthesis of ZnO structures by a simple wet chemical method, *Dig. J. Nanomater. BIOSTRUCTURES.* 8 (2013) 1591–1600.
- [27] V.R. Venu Gopal, S. Kamila, Effect of temperature on the morphology of ZnO nanoparticles: a comparative study, *Appl. Nanosci.* 7 (2017) 75–82, <https://doi.org/10.1007/s13204-017-0553-3>.
- [28] M.H. Hong, H. Choi, D. Il Shim, H.H. Cho, J. Kim, H.H. Park, Study of the effect of stress/strain of mesoporous Al-doped ZnO thin films on thermoelectric properties, *Solid State Sci.* 82 (2018) 84–91, <https://doi.org/10.1016/j.solidstatesciences.2018.05.010>.
- [29] S. Yasmeen, F. Iqbal, T. Munawar, M.A. Nawaz, M. Asghar, A. Hussain, Synthesis, structural and optical analysis of surfactant assisted ZnO–NiO nanocomposites prepared by homogeneous precipitation method, *Ceram. Int.* (2019) 1–15, <https://doi.org/10.1016/j.ceramint.2019.06.001>.
- [30] A. Khorsand Zak, W.H. Abd Majid, M.E. Abrishami, R. Yousefi, X-ray analysis of ZnO nanoparticles by Williamson-Hall and size-strain plot methods, *Solid State Sci.* 13 (2011) 251–256, <https://doi.org/10.1016/j.solidstatesciences.2010.11.024>.
- [31] V. Mote, Y. Purushotham, B. Dole, Williamson-Hall analysis in estimation of lattice strain in nanometer-sized ZnO particles, *J. Theor. Appl. Phys.* 6 (2012) 2–9, <https://doi.org/10.1186/2251-7235-6-6>.
- [32] X. Wang, T. Sun, H. Zhu, T. Han, J. Wang, H. Dai, Roles of pH, cation valence, and ionic strength in the stability and aggregation behavior of zinc oxide nanoparticles, *J. Environ. Manag.* 267 (2020) 110656, <https://doi.org/10.1016/j.jenvman.2020.110656>.
- [33] A. Anžlovar, K. Kogej, Z.C. Orel, M. Žigon, Impact of inorganic hydroxides on ZnO nanoparticle formation and morphology, *Cryst. Growth Des.* 14 (2014) 4262–4269, <https://doi.org/10.1021/cg401870e>.
- [34] Y. Im, S. Kang, B.S. Kwak, K.S. Park, T.W. Cho, J.S. Lee, M. Kang, Electrochemical performance of three shaped ZnO nanoparticles prepared in LiOH, NaOH and KOH alkaline solutions as anodic materials for Ni/Zn redox batteries, *Kor. J. Chem. Eng.* 33 (2016) 1447–1455, <https://doi.org/10.1007/s11814-015-0280-y>.
- [35] Z. Ait Abdelouhab, D. Djouadi, A. Chelouche, L. Hammiche, T. Touam, Effects of precursors and caustic bases on structural and vibrational properties of ZnO nanostructures elaborated by hydrothermal method, *Solid State Sci.* 89 (2019) 93–99, <https://doi.org/10.1016/j.solidstatesciences.2019.01.001>.
- [36] N. Uekawa, R. Yamashita, Y.J. Wu, K. Kakegawa, Effect of alkali metal hydroxide on formation processes of zinc oxide crystallites from aqueous solutions containing Zn(OH)<sub>4</sub><sup>2-</sup> ions, *Phys. Chem. Chem. Phys.* 6 (2004) 442–446, <https://doi.org/10.1039/b310306d>.
- [37] R. Wahab, S.G. Ansari, Y.S. Kim, M. Song, H.S. Shin, The role of pH variation on the growth of zinc oxide nanostructures, *Appl. Surf. Sci.* 255 (2009) 4891–4896, <https://doi.org/10.1016/j.apsusc.2008.12.037>.
- [38] Z. Ait Abdelouhab, D. Djouadi, A. Chelouche, L. Hammiche, T. Touam, Structural and morphological characterizations of pure and Ce-doped ZnO nanorods hydrothermally synthesized with different caustic bases, *Mater. Sci. Pol.* 38 (2020) 228–235, <https://doi.org/10.2478/msp-2020-0038>.
- [39] L. Tong, W. Li, O. Shen, H. Rong, L. Gong, Microwave-assisted the facile synthesis and photocatalytic properties of rhombic ZnO microstructures, *Mater. Lett.* 218 (2018) 1–4, <https://doi.org/10.1016/j.matlet.2018.01.134>.
- [40] P. Sadhukhan, M. Kundu, S. Rana, R. Kumar, J. Das, P.C. Sil, Microwave induced synthesis of ZnO nanorods and their efficacy as a drug carrier with profound anticancer and antibacterial properties, *Toxicol. Reports* 6 (2019) 176–185, <https://doi.org/10.1016/j.toxrep.2019.01.006>.
- [41] D.S. Chauhan, C.S.A. Gopal, D. Kumar, N. Mahato, M.A. Quraishi, M.H. Cho, Microwave induced facile synthesis and characterization of ZnO nanoparticles as efficient antibacterial agents, *Mater. Discov.* 11 (2018) 19–25, <https://doi.org/10.1016/j.md.2018.05.001>.
- [42] H. Noma, Y. Miwa, I. Yokoyama, K. Machida, Infrared and Raman intensity parameters of sodium acetate and their intensity distributions, *J. Mol. Struct.* 242 (1991) 207–219, [https://doi.org/10.1016/0022-2860\(91\)87136-6](https://doi.org/10.1016/0022-2860(91)87136-6).
- [43] M. Darvishi, F. Jamali-Paghaleh, M. Jamali-Paghaleh, J. Seyed-Yazdi, Facile synthesis of ZnO/rGO hybrid by microwave irradiation method with improved photoactivity, *Surfaces and Interfaces* 9 (2017) 167–172, <https://doi.org/10.1016/j.surfin.2017.09.008>.
- [44] A. Pimentel, J. Rodrigues, P. Duarte, D. Nunes, F.M. Costa, T. Monteiro, R. Martins, E. Fortunato, Effect of solvents on ZnO nanostructures synthesized by solvothermal method assisted by microwave radiation: a photocatalytic study, *J. Mater. Sci.* 50 (2015) 5777–5787, <https://doi.org/10.1007/s10853-015-9125-7>.
- [45] Sukriti, P. Chand, V. Singh, Enhanced visible-light photocatalytic activity of samarium-doped zinc oxide nanostructures, *J. Rare Earths* 38 (2020) 29–38, <https://doi.org/10.1016/j.jre.2019.02.009>.
- [46] S. Gao, F. Yang, C. Song, Q. Cai, R. Wang, S. Zhou, Y. Kong, Photocatalytic producing dihydroxybenzenes from phenol enabled by gathering oxygen vacancies in ultrathin porous ZnO nanosheets, *Appl. Surf. Sci.* 505 (2020) 144580, <https://doi.org/10.1016/j.apsusc.2019.144580>.
- [47] D. Liu, Y. Lv, M. Zhang, Y. Liu, Y. Zhu, R. Zong, Y. Zhu, Defect-related photoluminescence and photocatalytic properties of porous ZnO nanosheets, *J. Mater. Chem. A* 2 (2014) 15377–15388, <https://doi.org/10.1039/c4ta02678k>.
- [48] H. Vahdat Vasei, S.M. Masoudpanah, M. Habibollahzadeh, Different morphologies of ZnO via solution combustion synthesis: the role of fuel, *Mater. Res. Bull.* 125 (2020), <https://doi.org/10.1016/j.materresbull.2020.110784>.
- [49] A.P. Shah, S. Jain, V.J. Mokale, N.G. Shimpi, High performance visible light photocatalysis of electrospun PAN/ZnO hybrid nanofibers, *J. Ind. Eng. Chem.* 77 (2019) 154–163.
- [50] R.M. Jagtap, D.R. Kshirsagar, V.H. Khire, S.K. Pardeshi, Facile fabrication of porous La doped ZnO granular nanocrystallites and their catalytic evaluation towards thermal decomposition of ammonium perchlorate, *J. Solid State Chem.* 276 (2019) 194–204, <https://doi.org/10.1016/j.jssc.2019.05.001>.
- [51] R. López, R. Gómez, Band-gap energy estimation from diffuse reflectance measurements on sol-gel and commercial TiO<sub>2</sub>: a comparative study, *J. Sol. Gel Sci. Technol.* 61 (2012) 1–7, <https://doi.org/10.1007/s10971-011-2582-9>.
- [52] M.A. Alvi, A.A. Al-Ghamdi, M. Shaheer Akhtar, Synthesis of ZnO nanostructures via low temperature solution process for photocatalytic degradation of rhodamine B dye, *Mater. Lett.* 204 (2017) 12–15, <https://doi.org/10.1016/j.matlet.2017.06.005>.
- [53] F. Izquierdo De La Cruz, G. Pérez Hernández, F. Rodríguez Melgarejo, M.L. Ruiz Peralta, R. Castillo Palomera, E. Ramírez Morales, L. Rojas Blanco, SYNTHESIS ASSISTED BY MICROWAVE OF ZnO/ZnS/CuS HETEROSTRUCTURES AND ITS PHOTOACTIVITY USING VISIBLE LIGHT FOR DYES DEGRADATION, *Appl. Ecol. Environ. Res.* 16 (2018) 5745–5756.
- [54] J. Wang, Y. Xia, Y. Dong, R. Chen, L. Xiang, S. Komarneni, Defect-rich ZnO nanosheets of high surface area as an efficient visible-light photocatalyst, *Appl. Catal. B Environ.* 192 (2016) 8–16, <https://doi.org/10.1016/j.apcatb.2016.03.040>.
- [55] K. Karthik, S. Dhanuskodi, C. Gobinath, S. Prabukumar, S. Sivaramkrishnan, Multifunctional properties of microwave assisted CdO–NiO–ZnO mixed metal oxide nanocomposite: enhanced photocatalytic and antibacterial activities, *J. Mater. Sci. Mater. Electron.* 29 (2018) 5459–5471, <https://doi.org/10.1007/s10854-017-8513-y>.